

# Temperature dependence of excitonic recombination in lateral epitaxially overgrown InGaN/GaN quantum wells studied with cathodoluminescence

S. Khatsevich and D. H. Rich<sup>a)</sup>

*Department of Physics, Ben-Gurion University of the Negev, P.O.B. 653, Beer-Sheva 84105, Israel*

X. Zhang, W. Zhou, and P. D. Dapkus<sup>b)</sup>

*Department of Materials Science and Engineering, University of Southern California, Los Angeles, California 90089-0241*

(Received 25 August 2003; accepted 21 November 2003)

We have examined in detail the optical properties of InGaN quantum wells (QWs) grown on pyramidal GaN mesas prepared by lateral epitaxial overgrowth (LEO) in a metalorganic chemical vapor deposition system that resulted in QWs on  $\{1-101\}$  facets. The effects of In migration during growth on the resulting QW thickness and composition were examined with transmission electron microscopy (TEM) and various cathodoluminescence (CL) imaging techniques, including CL wavelength imaging and activation energy imaging. Spatial variations in the luminescence efficiency, QW interband transition energy, thermal activation energy, and exciton binding energy were probed at various temperatures. Cross-sectional TEM was used to examine thickness variations of the InGaN/GaN QW grown on a pyramidal mesa. CL imaging revealed a marked improvement in the homogeneity of CL emission of the LEO sample relative to a reference sample for a conventionally grown  $\text{In}_{0.15}\text{Ga}_{0.85}\text{N}/\text{GaN}$  QW. The characteristic phase separation that resulted in a spotty CL image profile and attendant carrier localization in the reference sample is significantly reduced in the LEO QW sample. Spatial variations in the QW transition energy, piezoelectric field, and thermal activation energy were modeled using excitonic binding and transition energy calculations based on a single-band, effective-mass theory using Airy function solutions. Band-edge and effective-mass parameters were first obtained from a strain- and In-composition-dependent  $k\cdot p$  calculation for wurtzite  $\text{In}_x\text{Ga}_{1-x}\text{N}$ , using a  $6\times 6$   $k\cdot p$  Hamiltonian in the  $\{1-101\}$  representations. The calculations and experiments confirm a facet-induced migration of In during growth, which results in a smooth compositional variation from  $x\approx 0.10$  at the bottom of the pyramid to  $x\approx 0.19$  at the top. We demonstrate the existence of a strong correlation between the observed thermal activation behavior of QW luminescence intensity and the associated exciton binding energy for various positions along the pyramidal InGaN/GaN QWs, suggesting exciton dissociation is responsible for the observed temperature dependence of the QW luminescence in the  $\sim 150$  to 300 K range. © 2004 American Institute of Physics. [DOI: 10.1063/1.1641146]

## I. INTRODUCTION

Progress in the development of blue-green light-emitting diodes and laser diodes has accelerated with the advent of epitaxial growth techniques that have realized high-quality, thick III-nitride films,<sup>1-3</sup> quantum heterostructures,<sup>3-5</sup> and selective doping of the ternary InGaN system.<sup>1-5</sup> Conventional vertical epitaxial techniques that employ standard sapphire substrates to achieve III-nitride growth result in films that usually exhibit a high threading dislocation density ( $10^8$ – $10^{10}\text{ cm}^{-2}$ ) and V defects, owing to the large lattice mismatch between wurtzite GaN and sapphire.<sup>6</sup> Most of the threading dislocations occur as a result of propagation from defects located near the surface of a GaN buffer layer, grown at low temperatures on the sapphire.<sup>6,7</sup> Additional complexities preventing the growth of smooth and homogeneous thin

InGaN films occur as a result of a miscibility gap at relevant growth temperatures.<sup>8-11</sup> The tendency of the films to decompose into distinct regions of inplane In- and Ga-rich phases has had a profound impact on the resulting optical properties and transport behavior. The behavior of excess electrons and holes is strongly affected by composition undulations that translate in localized confinement potentials, thereby directly influencing the carrier relaxation and transport and subsequent excitonic formation and recombination.<sup>12-15</sup> While it may be possible to exploit such phase separation in ternary films to achieve a desired dimensionality [e.g., zero (0D)- or one-dimensional (1D) regions], which enhances properties associated with exciton localization, radiative recombination, and lasing, there is clearly a desire to fabricate thin InGaN films and quantum wells (QWs) whose phase separation is minimal and in-plane In composition homogeneous.

A growth approach that has recently shown great promise in reducing the threading dislocation density in thick films to a level of  $\sim 10^4\text{ cm}^{-2}$  in GaN is the method of

<sup>a)</sup>Electronic mail: danrich@bgumail.bgu.ac.il

<sup>b)</sup>Also with Compound Semiconductor Laboratory, Department of Electrical Engineering/Electrophysics, University of Southern California, Los Angeles, California 90089-0241.

lateral epitaxial overgrowth (LEO).<sup>16–20</sup> In LEO, a dielectric mask is deposited over a starting GaN buffer layer that may contain a relatively high defect density. The mask is patterned using standard photolithography and reactive ion etching to create selective openings in the mask that possess a desired geometry or orientation relative to the GaN. Subsequent GaN growth then occurs in the opening in both vertical and lateral directions over the dielectric mask, thereby minimizing the vertical propagation of threading dislocations attendant in the GaN growth on an as-prepared, low-temperature buffer layer. Having achieved relatively defect-free regions of GaN, subsequent growth of higher quality InGaN/GaN QWs can be performed.<sup>21,22</sup> In this article, we report on the spatial variation in optical properties of InGaN/GaN QWs prepared using LEO. In particular, we examine a case in LEO growth in which the resulting shape of the LEO structure is pyramidal, having facet orientations of  $\{1-101\}$  that are not parallel to the (0001) plane of the starting GaN buffer layer. The effects of In migration during growth on the resulting QW composition and thickness were examined with low-temperature cathodoluminescence (CL) imaging and spectroscopy. Spatial variations in the QW transition energy, piezoelectric field, and thermal activation energy were modeled using excitonic binding and transition energy calculations based on a single-band, effective-mass theory. In this work, we aim to understand the underlying processes behind the thermal activation behavior of the InGaN/GaN QW luminescence intensity and its measured spatial variations.

## II. EXPERIMENT

The growth of pyramidal GaN structures on *c*-plane (0001) sapphire using LEO has been described previously in detail.<sup>19,22</sup> Briefly, metalorganic chemical vapor deposition (MOCVD) was used to grow GaN buffer layers on the sapphire substrate, followed by deposition of a 170-nm-thick SiN<sub>x</sub> mask using plasma-enhanced CVD. Conventional photolithography and reactive ion etching were used to form patterned stripes along the [11-20] direction, possessing openings with widths of 4 μm and pitch of 10 μm. The LEO GaN was then grown over the SiN<sub>x</sub> mask at a temperature of 1000 °C for ~1 h, resulting in pyramidal stripes possessing  $\{1-101\}$  sidewalls. Subsequently, a nominal 4-nm-thick In<sub>0.15</sub>Ga<sub>0.85</sub>N QW at 775 °C was grown and capped with a 70-nm-thick GaN layer. The nominal 15% In composition represents an average composition for an InGaN film grown on a flat (0001) GaN buffer. We have prepared a reference sample without the SiN mask that contains a 4-nm-thick In<sub>0.15</sub>Ga<sub>0.85</sub>N QW on a flat (0001) GaN buffer layer, followed by a 70-nm-thick GaN capping layer.

The CL experiments were performed with a modified JEOL-5910 scanning electron microscope (SEM).<sup>23</sup> A GaAs:Cs photomultiplier tube (PMT) was used to detect the luminescence dispersed by a 0.25 m monochromator for CL imaging and spectroscopy. We corrected the measured CL spectral line shapes according to the spectral response of the PMT in the 350 to 700 nm range. We employed CL wavelength imaging (CLWI) to enable a spatial mapping of the peak energy of the emission from the InGaN QWs. CLWI is

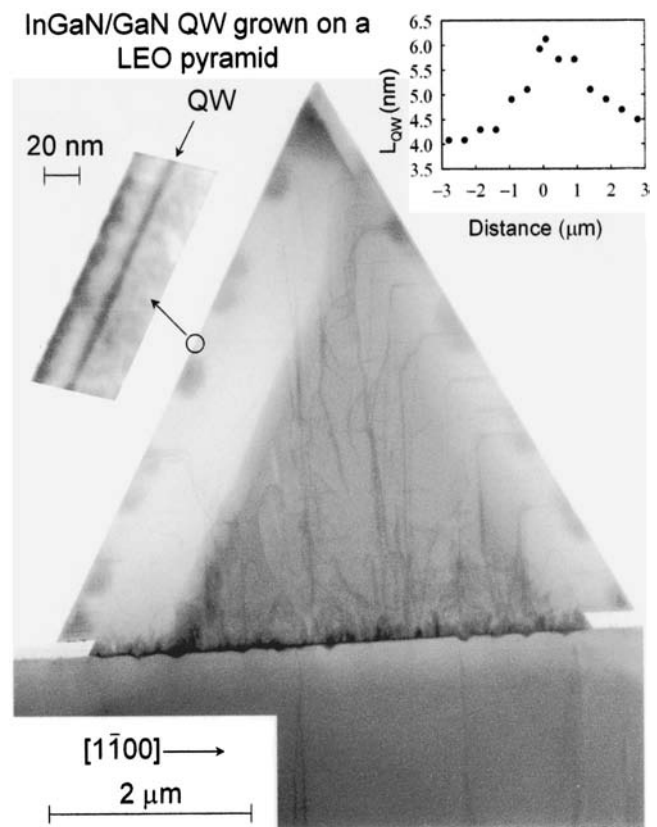


FIG. 1. Cross-sectional TEM image of a typical LEO-grown pyramidal mesa obtained along the [11-20] zone-axis, using bright-field detection. A higher magnification image of the InGaN/GaN QW is interposed, showing its corresponding length scale. An inset on the upper right shows a plot of the measured QW width ( $L_{QW}$ ) vs lateral distance along the [1-100] direction, where distance=0 is the position of the apex.

accomplished by acquiring a series of discrete monochromatic images, constructing a local spectrum at all 640×480 scan points within the image, and determining the wavelength  $\lambda_m(x,y)$  at which there is a peak in the CL spectrum at each scan point  $(x,y)$ .<sup>24</sup> Activation energy images (AEIs) are likewise obtained by measuring the change in the CL intensity versus temperature for each point  $(x,y)$ , determining the local activation energy at each point by a least-squares fit, and plotting a gray-scale intensity map that represents the activation energy.<sup>25</sup> Cross-sectional transmission electron microscopy (TEM) was performed using an Akashi EM-002B TEM. Bright-field images were acquired along the [11-20] zone axis, which is the direction of the GaN pyramidal stripes.

## III. RESULTS AND DISCUSSION

### A. TEM

A cross-sectional TEM image of a typical pyramidal mesa is shown in Fig. 1. Threading dislocations are observed to propagate vertically along [0001] from the interface of the buffer layer into the mesa. The dislocations eventually bend along the orthogonal [1-100] direction, prior to reaching the inclined  $\{1-101\}$  sidewalls. The quality of the mesa improves significantly at a level of 0.5 to 1 μm above the buffer layer interface. A higher magnification image in Fig. 1 shows the

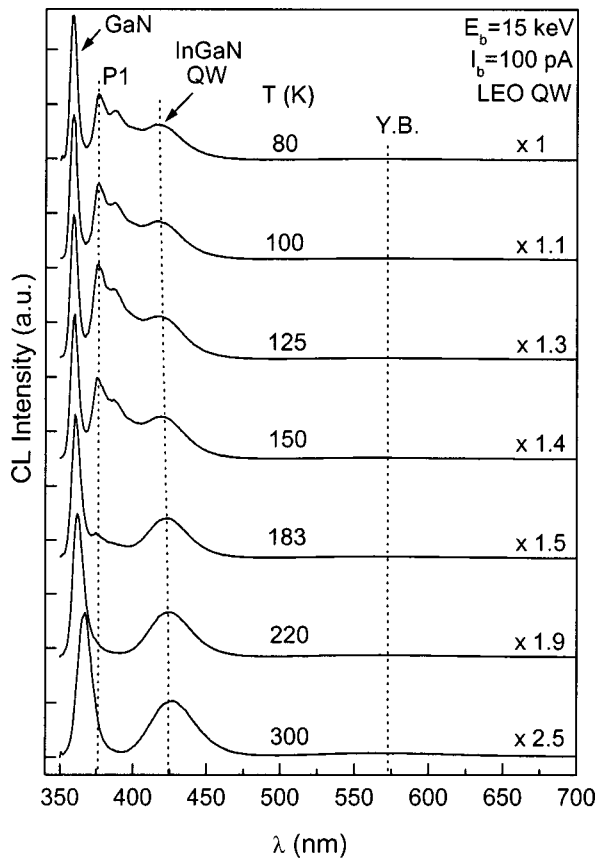


FIG. 2. Spatially averaged CL spectra at various temperatures acquired in the  $80 \leq T \leq 300$  K range for the patterned LEO InGaN/GaN QW sample. Different emission peaks and wavelength positions are indicated. The doublet labeled P1 is identified as a free-electron-to-acceptor transition in bulk GaN.

interfacial region between the QW and the GaN barrier. The darker regions in the image represent the  $\text{In}_x\text{Ga}_{1-x}\text{N}$  QW region. We have quantified the variation in the QW thicknesses by measuring the QW width versus the lateral distance (along the  $[1-100]$  direction) relative to the center of the pyramidal mesa. The results, shown as an inset in Fig. 1, indicate that the QW thickness increases nearly linearly from about 4.0 nm at the bottom of the mesa to  $\sim 6.0$  nm near the top.

### B. CL spectroscopy

Spatially averaged CL spectra of the patterned LEO sample were acquired while the electron beam was rastered over a  $64 \mu\text{m} \times 48 \mu\text{m}$  region for a beam energy of 15 keV and beam current of 100 pA, as shown in Fig. 2. Spectra were acquired for various temperatures from 80 to 300 K, as shown. All spectra are normalized to have nearly the same intensity; the scaling factors are indicated. Various peaks are identified as the near-band-edge GaN, yellow-band (Y-band) emission, and QW emission, as labeled in Fig. 2. The doublet labeled P1 located near 375 nm (3.30 eV) is identified as originating from a free-electron-to-acceptor transition in bulk GaN.<sup>26,27</sup> To confirm that this emission originates from GaN layers beneath the QW, we performed a depth-resolved analysis by acquiring CL spectra for various electron beam

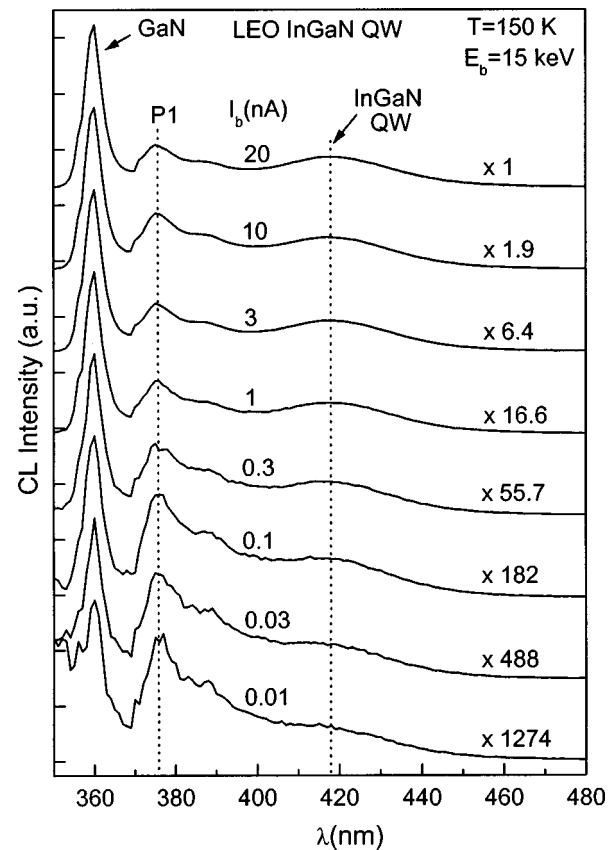


FIG. 3. Spatially averaged CL spectra for the patterned LEO InGaN/GaN QW sample at different probe currents  $I_b$  for  $T = 150$  K. The InGaN/GaN QW peak position is indicated by a vertical dashed line showing that the line shape remains constant over three orders of magnitude of excitation.

energies. For e-beam energies greater than  $\sim 10$  keV, the emission from the QW decreases rapidly relative to the P1 peak, indicating that the impurity related transition emanates mainly from GaN layers below the QW. The Y-band emission is similarly defect-related and correlates with the presence of threading dislocations and other related structural defects.<sup>28-30</sup>

In order to examine the possibility of state filling and excess-carrier-induced screening of the piezoelectric fields, we have examined the CL spectra for various e-beam currents, as shown in Fig. 3. Since the line shape remains constant over three orders of magnitude of excitation, we can assume that carrier filling and screening are negligible in the LEO sample under the present excitation conditions. The steady-state carrier density in the QW is related to the beam current by  $n_{\text{QW}} \approx 2.3 \times 10^{12} I_b$  ( $\text{cm}^{-2}$ ), where  $I_b$  is in nanoamperes.<sup>31,32</sup> CL results for the reference  $\text{In}_x\text{Ga}_{1-x}\text{N}/\text{GaN}$  QW sample with nominal composition  $x = 0.15$  are shown in Fig. 4. A blueshift of  $\sim 38$  meV in the QW peak is evident as  $I_b$  increases from 10 pA to 20 nA. The full widths at half-maximum of these spectra likewise increase from 80 to 92 meV over this range. Previously, this shift was attributed to carrier filling effects in phase-separated regions, which have locally higher In compositions.<sup>15</sup> The absence of such a blueshift in the LEO sample is an indication that the local structure is different, and immediately suggests an absence of the same phase

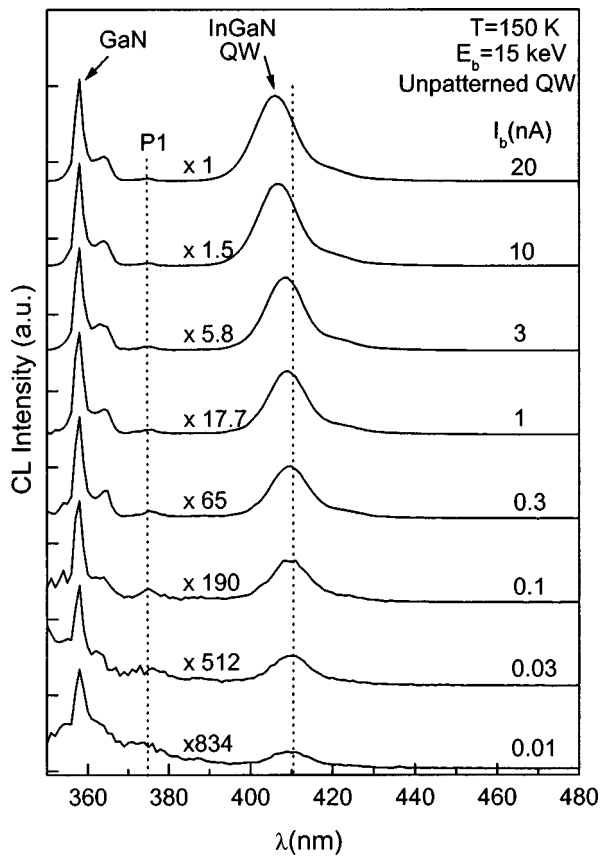


FIG. 4. Spatially averaged CL spectra for the reference unpatterned InGaN/GaN QW sample at different probe currents. A vertical dashed line indicates a blueshift in the InGaN/GaN QW peak position as  $I_B$  increases from 10 pA to 20 nA.

separation present in the reference QW sample. Such phase segregation creates local potential fluctuations that are highly susceptible to rapid state filling as the excitation is increased.<sup>12,15</sup>

In order to examine the temperature dependence of the QW emission intensity for the two samples, a semi-logarithmic plot of the CL intensity versus temperature is shown in Fig. 5. The electron beam was rastered over a  $64 \mu\text{m} \times 48 \mu\text{m}$  region for both samples during the CL intensity measurements, thereby giving a spatially averaged CL measurement. The CL intensity values in Fig. 5 represent an *absolute* CL emission comparison between the reference and LEO samples. The data show that the luminescence efficiency in the LEO sample is about two orders of magnitude greater than that of the reference sample for the measured temperatures, thereby demonstrating the marked enhancement in the material quality and reduction in average defect density for the LEO-grown sample. The results yield spatially averaged activation energies of 39 and 34 meV for the unpatterned and LEO QW samples, respectively, in the 150 to 300 K temperature range. For the lower temperature range (80 to 140 K), a change in the slope of the CL intensity versus temperature is observed, and yields activation energies of 18 and 8 meV for the unpatterned and LEO QW samples, respectively. Again, we expect that differences in local structure between the two samples ought to affect the nature of exciton dissociation. We will attempt to explain

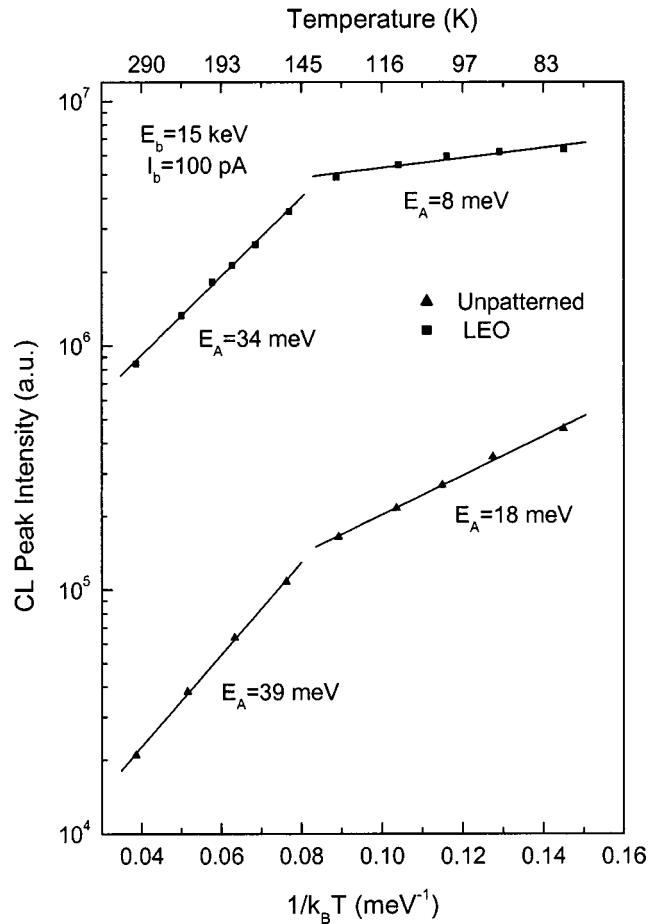


FIG. 5. A semi-logarithmic plot of the integrated CL intensity for the LEO sample (squares) and the reference QW sample (triangles) vs  $1/T$ , which exhibits an Arrhenius behavior. The electron beam was rastered over a  $64 \mu\text{m} \times 48 \mu\text{m}$  region for both samples during the measurement. Solid lines indicate the results of linear fits, from which corresponding activation energies are determined, as shown.

these differences in terms of observed differences in the In compositional variations between the LEO and conventionally grown samples.

### C. Monochromatic CL imaging, CLWI, and AEI

A conventional SEM image along with scanning monochromatic images at various wavelengths are shown in Fig. 6 over the same  $64 \mu\text{m} \times 48 \mu\text{m}$  region of the LEO sample. The spatial distribution of the luminescence varies according to the wavelength as a result of the compositional and well width variations across the pyramid. The TEM results further lead to the anticipated redshift of QW emission near the mesa top since the QW width increases from the bottom to the top of the pyramid. Likewise, the Y-band emission ( $\lambda = 565 \text{ nm}$ ) is observed localized near the top of the pyramid, consistent with the expectation that a higher density of threading dislocations are found over the window region of SiN mask relative to the sidewalls *over* the SiN mask,<sup>17–19</sup> thereby allowing for the vertical propagation of these defects to reach the top and affect the ensuing electron–hole recombination. In Fig. 7, the CLWI and AEI are shown below a

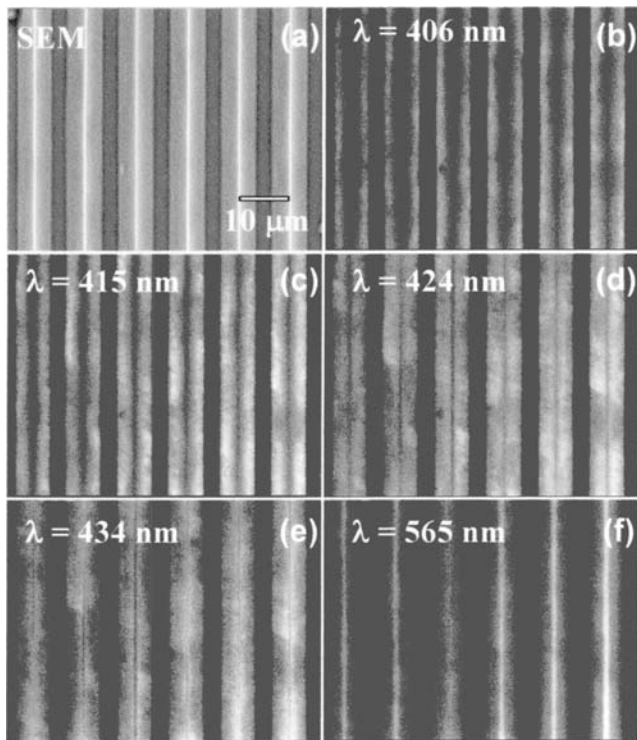


FIG. 6. SEM image (a), and monochromatic CL images for the LEO InGaN/GaN QW sample at various wavelengths:  $\lambda=406$  nm (b),  $\lambda=415$  nm (c),  $\lambda=424$  nm (d),  $\lambda=434$  nm (e), and  $\lambda=565$  nm (Y-band emission) (f). The e-beam excitation conditions were  $E_B=15$  keV and  $I_B=125$  pA at  $T=166$  K, with the electron beam rastered over a  $64\ \mu\text{m}\times 48\ \mu\text{m}$  region. The length scale for images (a)–(f) is indicated in the SEM image.

scanning monochromatic image at  $\lambda=417$  nm. Temperatures in the range of 150 to 200 K were used to construct the AEI.

In order to better observe the existing spatial correlations between CL intensity  $I_{CL}$ , activation energy  $E_A$ , peak emission wavelength  $\lambda_m$ , Y-band, and secondary electron intensity (i.e.,  $I_{SE}$ , the SEM imaging intensity), a binning of pixels along an arbitrary horizontal line in the images of Figs. 6 and 7 permits, respectively, a 1D representation of  $I_{CL}$ ,  $E_A$ ,  $\lambda_m$ , Y-band, and  $I_{SE}$  versus linear distance  $l$  in Fig. 8. The apexes of the pyramid are identified by the peaks of  $I_{SE}$  in Fig. 8(e), and are seen to correlate spatially with a peak in  $\lambda_m$ , Y-band, and  $E_A$ . From the lower edges of the pyramids,  $\lambda_m$ ,  $E_A$ ,  $I_{CL}$ , and Y-band increase from the bottom to the top. There is a noticeable dip in  $I_{CL}$  as the electron beam approaches the apex. This dip, as observed before, is correlated with the presence of Y-band emission and is likely caused by threading dislocations that have reached the top of the pyramid. The combination of the additional Y-band channels and *nonradiative* channels are sufficient to cause the observed decrease in the luminescence efficiency of the QW.<sup>33,34</sup>

The relative increase in  $\lambda_m$ ,  $E_A$ , and  $I_{CL}$  near the apex suggests a strong connection with an increase in both QW width ( $L_{QW}$ ) and In composition  $x$ , near the apex. While an increase in  $\lambda_m$  is directly related to an increase in  $L_{QW}$  and  $x$ , additional considerations are needed to explain the behavior of  $E_A$ , and  $I_{CL}$  versus  $l$ . A set of images in Fig. 9 that were obtained at higher magnification illustrate the existence of

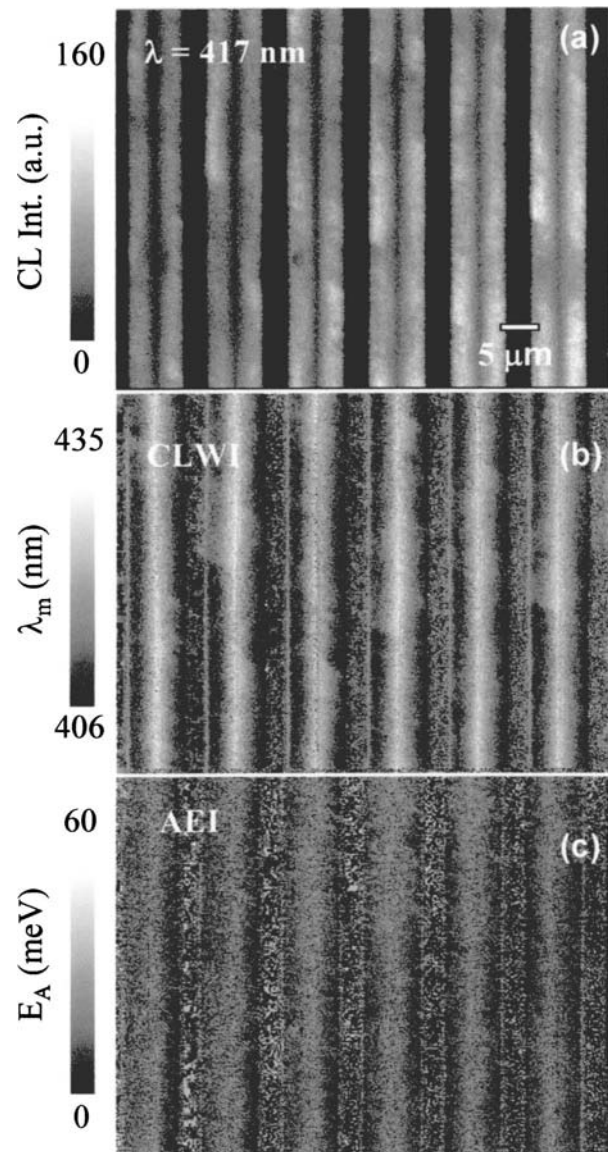


FIG. 7. A set of images obtained with an electron beam of  $E_B=15$  keV and  $I_B=125$  pA over a  $64\ \mu\text{m}\times 48\ \mu\text{m}$  region for the LEO InGaN/GaN QW sample: monochromatic CL image at  $\lambda=417$  nm and  $T=166$  K (a), CLWI image at  $T=300$  K (b), and AEI constructed in the temperature range of 150 to 200 K (c). The length scale for all images (a)–(c) is indicated in the CL image.

some micrometer-scale variations in  $\lambda_m$ ,  $E_A$ , and  $I_{CL}$ . Various surface imperfections on the GaN pyramid, as observed in the SEM image of Fig. 9(b), may partially explain such variations. Two large imperfections are indicated by dashed arrows. Smaller imperfections, while not visible under the current SEM imaging conditions, may influence the details of the In *cation migration* giving rise to such variations. Spatial variations are further accentuated in the AEI of Fig. 9(e), by employing a detection window about 10 nm off the nominal peak position of  $\lambda=420$  nm since small changes in  $\lambda_m$  will bring about larger relative variations in  $I_{CL}(T)$  when the wavelength detection window deviates from  $\lambda_m$ . Before providing a detailed model of the AEI behavior, it is first necessary to consider a similar CL imaging analysis of the unpatterned referenced sample.

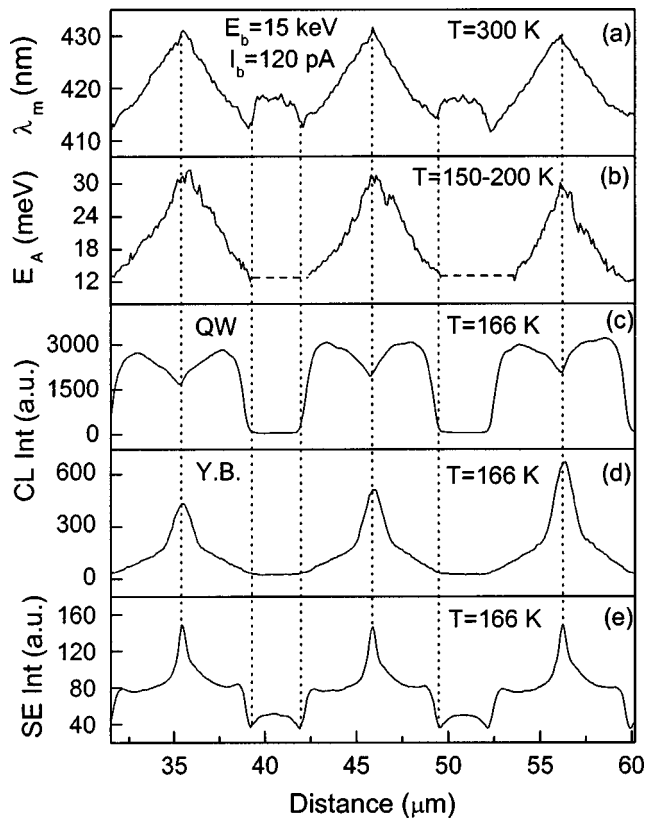


FIG. 8. Line-scan analysis for the LEO InGaN/GaN QW sample showing (a) the peak wavelength  $\lambda_m$ , (b) activation energy  $E_A$ , (c) integrated CL intensity of QW emission, (d) integrated CL intensity of Y-band emission and (e) secondary electron intensity versus distance along an arbitrary line in [1-100] direction. The vertical dashed lines illustrate the spatial correlation between peaks and dips of these scans.

CL imaging results for the reference QW sample are shown in Figs. 10 and 11, respectively. The images of  $\lambda_m$ ,  $E_A$ , and  $I_{CL}$  are shown in Fig. 10 and illustrate the spotty nature of the InGaN QW growth on the GaN layers. The distinct bright and dark regions of emission are consistent with a strong localization of excitons prior to radiative recombination.<sup>15</sup> The AEI appears similar to the monochromatic image, yet the information contained in these images is very different. Again, the AEI, like that of the patterned sample, was obtained by acquiring images in the 150 to 200 K range and extracting the activation energy at each point by linear fits. A 1D plot of this data is shown in Fig. 11, and the vertical dashed lines help illustrate the strong correlation between peaks and dips for each of the parameters  $\lambda_m$ ,  $E_A$ , and  $I_{CL}$ . These results are consistent with the lateral bandgap variation that accompanies phase separation into In- and Ga-rich regions of the QW. The positive correlation between  $\lambda_m$ ,  $E_A$ , and  $I_{CL}$  is understood through a simple model in which In-rich regions naturally lead to a smaller QW bandgap that will induce an increase in the collected local carrier density and lead to an increased CL intensity. Likewise, the decrease in QW bandgap in In-rich regions will increase the exciton localization, resulting in a greater thermal energy required for exciton dissociation that is reflected by the larger  $E_A$ . In comparison with the corresponding images for LEO growth in Figs. 6–9, the local spatial variations in  $\lambda_m$ ,

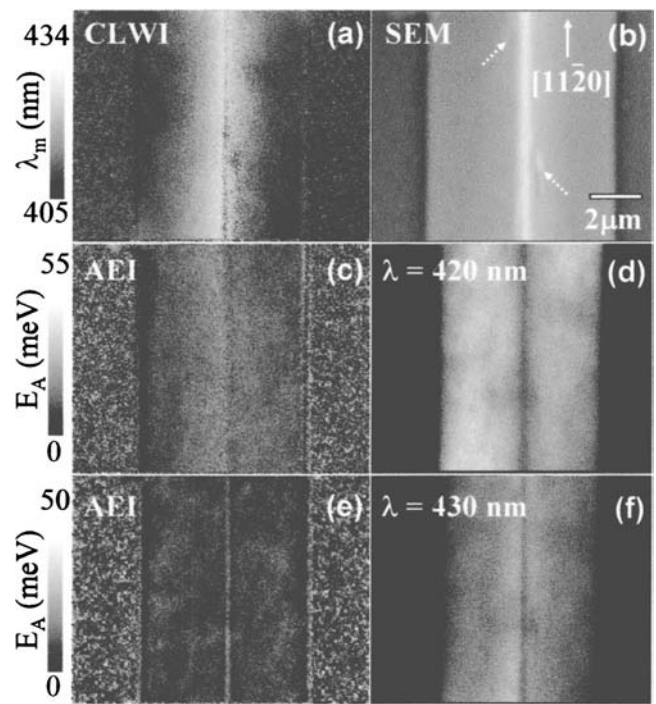


FIG. 9. A set of images obtained with an electron beam of  $E_B = 15$  keV and  $I_B = 125$  pA over a  $12.8 \mu\text{m} \times 9.6 \mu\text{m}$  region for the LEO InGaN/GaN QW sample: CLWI image (a), SEM image (b), AEI and CL image at  $\lambda = 420$  nm (c) and (d), and AEI and CL image at  $\lambda = 430$  nm (e) and (f). Temperatures in the range of 150 to 200 K were used to construct AEI. Two large surface imperfections are indicated by dashed arrows in the SEM image (b).

$E_A$ , and  $I_{CL}$  for the LEO sample are evidently reduced significantly relative to that for the reference sample, owing to the estimated ~four orders of magnitude reduction in threading dislocation density and reduced In phase segregation expected for the LEO sample.

We also note that CL imaging further reveals that the size of the In- and Ga-rich regions (bright and dark spots, respectively) in the reference sample depends on the level of excitation. The minimum feature size scales by a factor of ~2 as the beam current is increased from 0.3 to 1 nA at a beam energy of 10 keV. The increase in the feature size is evidently related to the rapid band filling of carriers in the In-rich regions which, in turn, change the shape of the potential variation in the vicinity of the In-rich center owing to screening. The resulting drift and diffusion of carriers towards the local minima are therefore altered and result in the excitation dependence of the CL feature sizes.

#### D. Model for spatial variations in exciton binding energy and interband transition energy

In order to model the observed variations in the interband transition energies, exciton binding energies, and thermal activation behavior, we have employed a single-band, effective-mass approximation in the calculation of the electron and hole eigenstates of the  $\text{In}_x\text{Ga}_{1-x}\text{N}/\text{GaN}$  QW. We have first employed a full  $k \cdot p$  perturbation method that is appropriate for strained wurtzite semiconductors to calculate the bulk valence-band (VB) dispersions and hole effective masses for dispersion along the relevant  $\langle 1-101 \rangle$  directions,

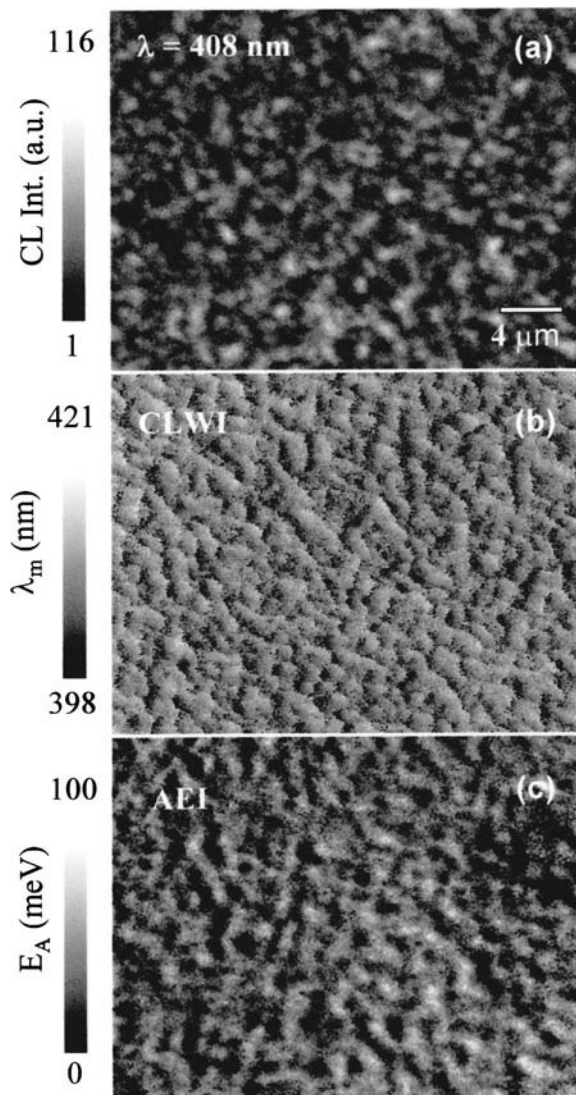


FIG. 10. A set of images obtained with an electron beam of  $E_B = 15$  keV and  $I_B = 130$  pA over the  $32 \mu\text{m} \times 24 \mu\text{m}$  region for the reference unpatterned InGaN/GaN QW sample: monochromatic CL image at  $\lambda = 408$  nm and  $T = 166$  K (a), CLWI image at  $T = 300$  K (b), and AEI constructed in the temperature range of 150 to 200 K (c). The length scale for all images (a)–(c) is indicated in the CL image.

which are normal to planes of the QW grown on the pyramidal faces.<sup>35,36</sup> The relevant parameters in the  $\mathbf{k}\cdot\mathbf{p}$  method for a wurtzite crystal include the  $A_i$ , which are similar to the Luttinger parameters in a zinc-blende crystal; the  $D_i$ , which are the deformation potentials for the  $\text{In}_x\text{Ga}_{1-x}\text{N}$  layers;  $c_{ij}$ , which are the elastic constants, and  $\epsilon_{ij}$ , the strain tensor components, which are appropriate for our pseudomorphically grown QWs on the  $\{1-101\}$  faces.<sup>35</sup> The  $\mathbf{k}\cdot\mathbf{p}$  calculation was performed by transforming the  $6 \times 6$  Hamiltonian for the VB structure in the wurtzite crystal from the (0001) orientation into the appropriate strain-dependent Hamiltonian for a biaxial stress in the  $\{1-101\}$  plane of the QW grown on the pyramidal sidewall. The  $\mathbf{k}\cdot\mathbf{p}$  parameters for  $\text{In}_x\text{Ga}_{1-x}\text{N}$  were obtained by linearizing between those for InN and GaN for a given composition  $x$ . The unstrained  $\text{In}_x\text{Ga}_{1-x}\text{N}$  bandgap at the room temperature is  $E_g = 3.44 - 3x$ .<sup>37</sup>

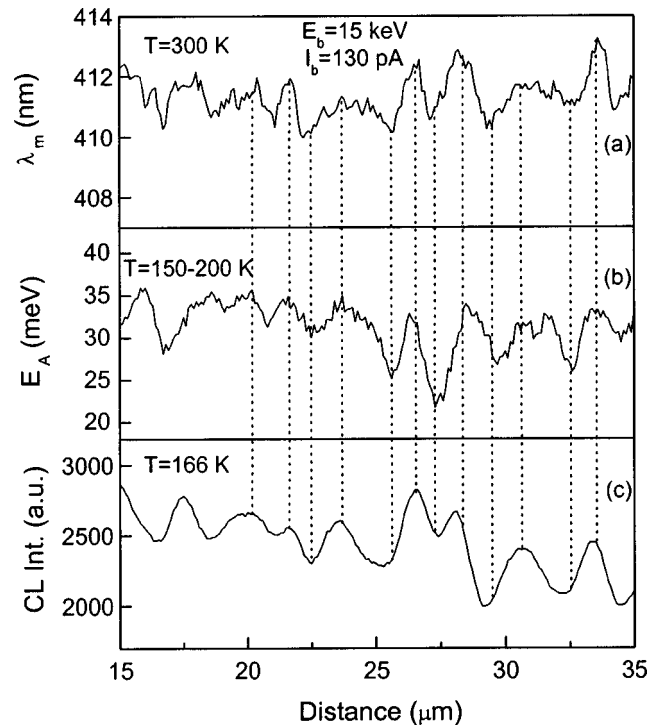


FIG. 11. Line-scan analysis of the reference unpatterned InGaN/GaN QW sample showing (a) the peak wavelength  $\lambda_m$  at  $T = 300$  K, (b) activation energies  $E_A$  constructed from data in the 150 to 200 K range and (c) integrated CL intensity ( $T = 166$  K) versus distance along an arbitrary line. The vertical dashed lines illustrate the spatial correlation between peaks and dips for these scans.

In Table I, we list the values that we employed in our  $\mathbf{k}\cdot\mathbf{p}$  calculation from the various referenced sources. The strain tensor components  $\epsilon_{ij}$ , along with the piezoelectric tensor elements  $d_{ijk}$ , and spontaneous polarization parameter  $P_{sp}$ , are also used to calculate the electric field  $F_{QW}$  experienced by electrons and holes in the QW. A spatial variation in the In composition  $x$  occurs as a result of the MOCVD growth on a nonplanar facet, leading to the diffusion and migration of In towards the top of the pyramidal mesa during growth,<sup>22</sup> as previously discussed. After a determination of the VB energy dispersions for a given In composition, the heavy-hole effective masses for dispersion along  $\langle 1-101 \rangle$  (i.e., the QW  $z$  direction),  $m_{hh}^z$ , and the average in-plane  $\{1-101\}$  effective masses,  $m_{hh}^{xy}$ , were determined and were found to be well approximated as linear functions of  $x$ . Our calculations yield  $m_{hh}^z = (1.48 + 0.13x)m_0$  and  $m_{hh}^{xy} = (0.80 + 0.77x)m_0$ . The electron effective masses for dispersion in the QW  $x$ - $y$  plane and along the QW  $z$  direction are obtained by a linearization between values for InN and GaN as  $m_e^{xy} = (0.23 - 0.13x)m_0$  and  $m_e^z = (0.19 - 0.08x)m_0$ .

Single-particle electron and hole wave functions  $\psi_{e,h}(z)$ , and ground state energies were determined by solutions to the Schrödinger equation for a particle subject to an electric field  $F_{QW}$ . The solutions involve linear combinations of Airy functions  $Ai(z)$  and  $Bi(z)$ .<sup>48,49</sup> We used a standard transfer matrix method (TMM) for these calculations.<sup>49,50</sup> The conduction to VB offset in wurtzite  $\text{In}_x\text{Ga}_{1-x}\text{N}$  is assumed to be independent of  $x$ , and is taken as  $\Delta E_c / \Delta E_v = 70/30$ .<sup>43,51</sup> The strain induced increase in the

TABLE I. Material constants used in the calculations.

	InN	GaN
$\epsilon$	15.3 <sup>a</sup>	8.9 <sup>a</sup>
$m_{e,l}(m_0)$	0.11 <sup>a</sup>	0.19 <sup>b</sup>
$m_{e,l}(m_0)$	0.10 <sup>a</sup>	0.23 <sup>b</sup>
$A_1$	-9.28 <sup>c</sup>	-6.56 <sup>d</sup>
$A_2$	-0.6 <sup>c</sup>	-0.91 <sup>d</sup>
$A_3$	8.68 <sup>c</sup>	5.65 <sup>d</sup>
$A_4$	-4.34 <sup>c</sup>	-2.83 <sup>d</sup>
$A_5$	-4.32 <sup>c</sup>	-3.13 <sup>d</sup>
$A_6$	-6.08 <sup>c</sup>	-4.86 <sup>d</sup>
$a_{c,l}$ (eV)	-4.08	-4.08 <sup>e</sup>
$a_{c,l}$ (eV)	-4.08	-4.08 <sup>e</sup>
$D_1$	0.7	0.7 <sup>e</sup>
$D_2$	2.1	2.1 <sup>e</sup>
$D_3$	1.4	1.4 <sup>e</sup>
$D_4$	-0.7	-0.7 <sup>e</sup>
$D_5$	-4	-4 <sup>e</sup>
$D_6$	-10.3	-10.3 <sup>e</sup>
$\Delta_1$ (meV)	41 <sup>f</sup>	16 <sup>e</sup>
$\Delta_2$	0.33 <sup>f</sup>	4 <sup>e</sup>
$\Delta_3$	0.33 <sup>f</sup>	4 <sup>e</sup>
$C_{11}$ (GPa)	223 <sup>g</sup>	370 <sup>h</sup>
$C_{12}$ (GPa)	115 <sup>g</sup>	145 <sup>h</sup>
$C_{13}$ (GPa)	92 <sup>g</sup>	110 <sup>h</sup>
$C_{33}$ (GPa)	224 <sup>g</sup>	390 <sup>h</sup>
$C_{44}$ (GPa)	48 <sup>g</sup>	90 <sup>h</sup>
$d_{31}$ (cm <sup>-2</sup> Pa <sup>-1</sup> )	-3.147 <sup>i</sup>	-1.253 <sup>i</sup>
$d_{33}$ (cm <sup>-2</sup> Pa <sup>-1</sup> )	6.201 <sup>i</sup>	2.291 <sup>i</sup>
$d_{15}$ (cm <sup>-2</sup> Pa <sup>-1</sup> )	-2.292 <sup>i</sup>	-1.579 <sup>i</sup>
$P_{sp}$ (C m <sup>-2</sup> )	-0.032 <sup>i</sup>	-0.029 <sup>i</sup>

<sup>a</sup>Reference 26.

<sup>b</sup>Reference 38.

<sup>c</sup>Reference 39.

<sup>d</sup>Reference 40.

<sup>e</sup>References 41, 42.

<sup>f</sup>Reference 43.

<sup>g</sup>Reference 44.

<sup>h</sup>Reference 45.

<sup>i</sup>References 46, 47.

bandgap is given by solutions from the  $k \cdot p$  calculations which included the deformation potentials for a particular strain tensor.

We have solved for the ground state wave function and binding energy of Wannier excitons which are assumed to be formed by electrons and holes in the In<sub>x</sub>Ga<sub>1-x</sub>N/GaN QW using the Airy function solutions just described. By utilizing the electron and hole wave functions from the TMM calculation, we reduce the two-body exciton problem into a radial eigenvalue equation that involves the electron-hole relative motion in an effective in-plane Coulomb potential.<sup>52</sup> The Hamiltonian of the exciton in a QW within the effective-mass approximation can be reduced to the following radial equation, which describes the relative in-plane exciton motion:

$$-\frac{\hbar^2}{2\mu} \frac{1}{r} \frac{d}{dr} \left( r \frac{d}{dr} \right) \phi_{e-h}(r) + V(r) \phi_{e-h}(r) = -E_B \phi_{e-h}(r), \quad (1)$$

where  $r$  is the relative in-plane coordinate,  $\mu$  is the reduced

mass of the electron-hole pair, and  $E_B$  is the exciton binding energy.<sup>52</sup>  $V(r)$  is the effective in-plane Coulomb potential, which is given by

$$V(r) = -\frac{e^2}{\epsilon} \int dz_e \int dz_h \frac{|\psi_e(z_e)|^2 |\psi_h(z_h)|^2}{\sqrt{r^2 + (z_e - z_h)^2}}, \quad (2)$$

where  $\epsilon$  is the background dielectric constant,  $z_e$  and  $z_h$  are the respective variables for the single-particle electron and hole wave functions  $\psi_{e,h}(z_{e,h})$ , obtained from the TMM procedure. The reduced mass  $\mu$  is obtained from the in-plane electron and hole masses for a given In composition  $x$ , as described earlier. The method of finite differences was used to solve the eigenvalue equation of Eq. (1) for  $E_B$ .

We further observe from Fig. 8, that the integrated intensity of CL emission from the QW sharply decreases for e-beam positions approaching the lower edge of the pyramid. We attribute this decrease to be due to a relative increase in the strain-induced piezoelectric field near the bottom of the pyramid which acts to separate spatially the electron and hole wave functions. We note that defects in the pyramid are primarily localized at the top of the pyramid and not at the bottom, as evidenced by the enhanced Y-band emission seen in the CL images of Figs. 6(f) and 8(d). This Y-band emission however is not prominent in the emission near the lower half of the pyramidal mesa, where the large decrease in the CL intensity  $I_{CL}$ , occurs. Thus, it appears most likely that a variation in the total field  $F_{QW}$ , along the pyramidal sidewalls causes the large variations in CL emission. Assuming a roughly constant effective carrier lifetime throughout the lower through middle regions of the QW on the pyramid, the integrated CL intensity  $I_{CL}(l)$  is given by  $I_{CL}(l) \propto \int dz \psi_e(z,l) \psi_h(z,l)^2$ , where  $l$  is the lateral distance from the mesa top.

We find that in order to reproduce the measured drop in  $I_{CL}$  observed in Fig. 8(c) near the bottom edge of the pyramid, it is necessary to assume a linear decrease in the field  $F_{QW}$  from the bottom to the top of the pyramid. By iteratively calculating  $\psi_e(z,l)$  and  $\psi_h(z,l)$  from the TMM, and comparing the overlap of the single-particle electron and hole wave functions with the spatial variation in  $I_{CL}(l)$ , we find that  $F_{QW}$  decreases approximately linearly from 1.0 to 0.08 MV/cm from regions near the bottom to the top of the pyramid; that is, from  $l=0$  to 3.75  $\mu\text{m}$ . Such a variation in field is evidently caused by a strain relaxation that also varies in a nearly linear fashion from the bottom to the top of the mesa. The TEM image of Fig. 1, which shows the enhanced propagation of threading dislocations near the top, together with the localization of Y-band emission near the top, suggests the existence of such a relaxation behavior through dislocations.<sup>25,28,33</sup> We show an example of  $|\psi_e(z,l)|^2$  and  $|\psi_h(z,l)|^2$  obtained from these calculations illustrated on the QW VB profile in Fig. 12 for a field  $F_{QW}=0.38$  MV/cm and distance  $l=2.5$   $\mu\text{m}$  from the lower edge of a pyramid.

In the simplest model that attempts to correlate structural and compositional variations in the QW with variations in the QW luminescence energies along the pyramid, we take both the In composition  $x$  and the QW width  $L_{QW}$  to vary linearly from the bottom to the top of the mesa. The latter

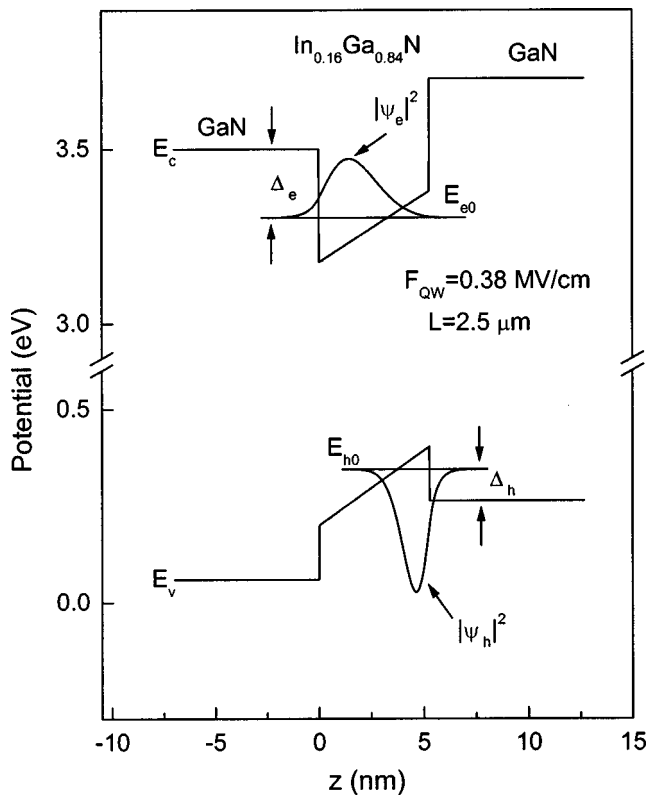


FIG. 12. The potential structure with plots of  $|\psi_e(z,l)|^2$  and  $|\psi_h(z,l)|^2$  for a strained wurtzite  $\text{In}_x\text{Ga}_{1-x}\text{N}/\text{GaN}$  QW grown on the  $\{1-101\}$  faces. An example is shown from our model which yields  $F_{\text{QW}}=0.38$  MV/cm and  $x=0.16$  at a distance  $l=2.5$   $\mu\text{m}$  from the lower edge of a pyramid. The ground state energy and effective barrier heights of electrons ( $E_{e0}, \Delta_e$ ) and holes ( $E_{h0}, \Delta_h$ ) are indicated.

assumption is supported by the TEM measurements, which showed a nearly linear variation in  $L_{\text{QW}}$  from 4.0 nm at the bottom to 6.0 nm at the top of the pyramid. The diffusion and migration of In on various *non-planar* facets during growth of various III-As and -N systems have been observed and have exhibited large lateral variations in the bandgap.<sup>53</sup> Thus, we have performed a series of iterative calculations that attempt to fit the CLWI data of Fig. 8(a) by calculating the interband transition energy and exciton binding energy through (i) a  $k\cdot p$  calculation of the In composition- and strain-dependent effective-mass and band-edge parameters, followed by (ii) the TMM calculation of  $\psi_e(z,l)$  and  $\psi_h(z,l)$  using Airy functions with the appropriate position-dependent fields, and (iii) calculation of the exciton binding energies  $E_B$ , which also depends on the position  $l$ . We allow only the composition  $x$  to vary linearly from the bottom to the top so as to minimize the difference between the measured and calculated interband transition energies of the QW. The primary constraints in this model are a linear variation in  $L_{\text{QW}}$  from 4.0 to 6.0 nm from the bottom to the top of the pyramid and a matching of  $|\int dz \psi_e(z,l) \psi_h(z,l)|^2$  with the spatial variation in  $I_{\text{CL}}$ , which yields the linear dependence of the field  $F_{\text{QW}}$  on position  $l$ .

The results of the calculations are shown in Fig. 13 for  $T=300$  K. The excitonic transition energy and excitonic binding energy are shown in the plots along with the measured QW luminescence energy from CLWI and the mea-

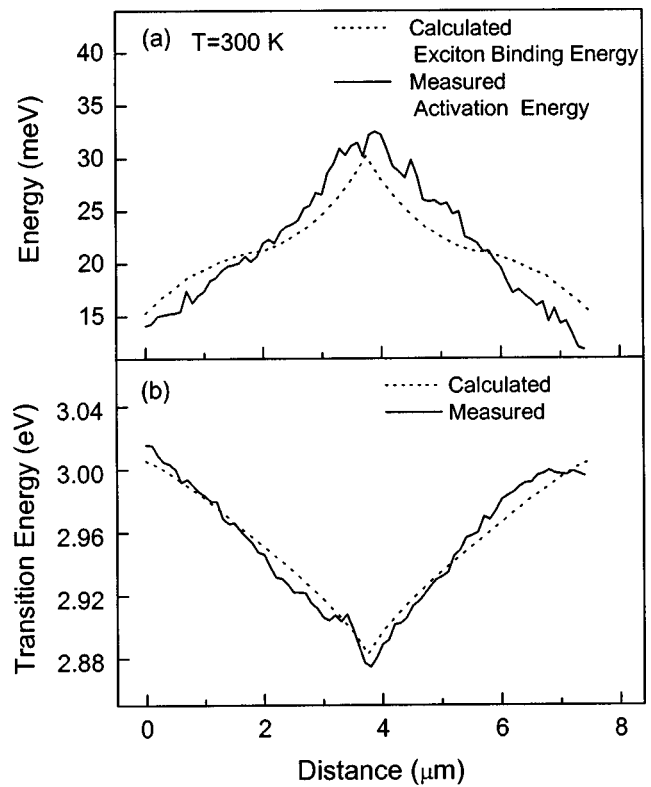


FIG. 13. Comparisons between calculated QW exciton binding energy (dotted line) with experimentally measured activation energy (solid line) from AEI vs position in (a) and calculated QW excitonic transition energy (dotted line) with experimentally measured QW luminescence energy (solid line) from CLWI versus position in (b).

sured CL activation energies  $E_A$  from AEI in the 150 to 200 K range (i.e., in the high-temperature range). These calculations yield a variation in  $x$  from 0.10 at the pyramidal bottom to 0.19 at the pyramidal top. All data in Fig. 13 is shown as a function of position  $l$  relative to the lower left edge of a pyramid.

The calculations confirm what has qualitatively been inferred from the CLWI results, namely, the large variation of about  $\pm 0.05$  in the In composition along the sidewalls of the pyramids from the nominal value of  $x=0.15$  during growth. The facet-dependent migration of cations on high-index crystal facets of III-V surfaces during growth is well documented.<sup>53,54</sup> Another fundamental conclusion drawn from the results relates to the strong correspondence between  $E_A$  and the calculated exciton binding energy  $E_B$ , as observed in Fig. 13(a). This correspondence strongly suggests that the observed thermal activation behavior in the integrated CL intensity for the high-temperature range of 150 to 300 K is caused by dissociation of the QW excitations according to the Boltzmann activation energy behavior; that is,  $I_{\text{CL}}^{-1} \propto \exp(-E_B/k_B T)$ . A previous common interpretation of thermal activation, as it relates to the change in  $I_{\text{CL}}$  versus  $T$ , is that electrons and holes are re-emitted from their respective ground states into continuum states of the barrier, thereby reducing the rate of electron-hole pair radiative recombination as the temperature is increased.<sup>25</sup> Previous temperature-dependent CL studies of InGaAs/GaAs QWs and quantum dots (QDs) have shown a strong similarity be-

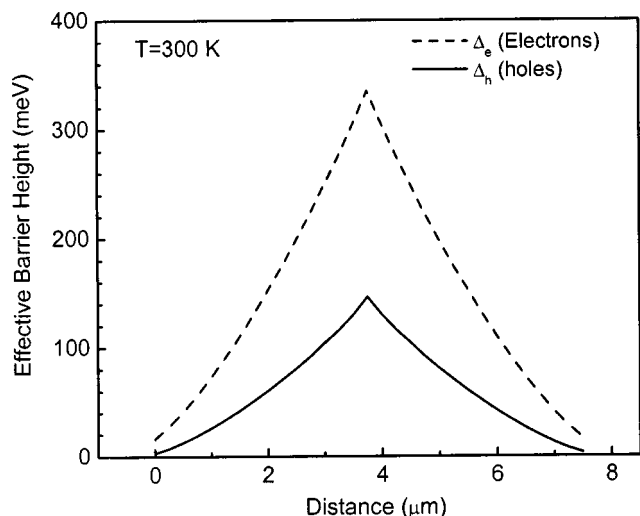


FIG. 14. The effective barrier heights of electrons ( $\Delta_e$ ) and holes ( $\Delta_h$ ) versus distance  $l$ , according to the model calculations.

tween the measured thermal activation energy and the calculated effective barrier heights of electrons and holes,  $\Delta_e$  and  $\Delta_h$ , respectively (i.e., the energy difference between the QW or QD ground state energies and the barrier levels),<sup>25,55</sup> as illustrated in Fig. 12 for our case. In order to consider the possibility of thermal re-emission over the effective barriers, we plot the effective barrier heights from our calculations for electrons ( $\Delta_e$ ) and holes ( $\Delta_h$ ) versus distance  $l$  in Fig. 14. Near the mesa top,  $\Delta_e$  and  $\Delta_h$  are 335 and 146 meV, respectively, in comparison to a measured activation energy  $E_A$  of  $\sim 34$  meV and calculated exciton binding energy of 30 meV. Thus, we conclude that thermal re-emission of carriers contributes negligibly to the observed thermal activation behavior involving  $I_{CL}$  versus  $T$ ; instead, exciton dissociation is the likely cause for such behavior in the present InGaN/GaN QWs.

Finally, the reduction in activation energies for the intermediate temperature range of 80 to 140 K apparently reflects the presence of local potential fluctuations caused by the In-phase segregation in the QWs. These potential fluctuations may lead to local carrier trapping and are expected to affect the details of exciton formation, including electron-hole confinement and dimensionality (i.e., two-dimensional versus 0D). The larger  $E_A$  in the unpatterned sample (18 meV) in comparison to that for the LEO sample (8 meV) is consistent with the larger phase segregation present in the unpatterned sample. It is also worth noting that potential fluctuations in the GaN barriers may impede carrier transfer to the QWs at lower temperatures, thereby effectively reducing the measured  $E_A$ . A similar low-temperature activation behavior was observed for  $\text{In}_{0.2}\text{Ga}_{0.8}\text{As}/\text{GaAs}$  multiple QWs, where a reduction in activation energy for  $T < \sim 150$  K was attributed to defects and potential fluctuations in the GaAs barriers, which reduced carrier collection in the QWs.<sup>25</sup>

#### IV. SUMMARY AND CONCLUSIONS

We have examined in detail the optical properties of InGaN QWs grown on pyramidal GaN mesas prepared by LEO

that resulted in QWs on  $\{1-101\}$  facets. The effects of In migration during growth on the resulting QW composition and thickness were examined with TEM and various CL imaging techniques, including CL wavelength imaging and AEI (activation energy imaging). Spatial variations in the luminescence efficiency, QW interband transition energy, thermal activation energy, and exciton binding energy were probed at various temperatures. CL imaging revealed a marked improvement in the homogeneity of CL emission of the LEO sample relative to a reference sample for a conventionally grown InGaN/GaN QW. The characteristic phase separation that resulted in a spotty CL image profile and attendant carrier localization in the reference sample is significantly reduced in the LEO QW sample. Spatial variations in the QW transition energy, piezoelectric field, and thermal activation energy were modeled using excitonic binding and transition energy calculations based on a single-band, effective-mass theory. The calculations employed band-edge parameters obtained from a strain- and In-composition-dependent  $k\cdot p$  calculation for wurtzite  $\text{In}_x\text{Ga}_{1-x}\text{N}$  with the  $6\times 6$  valence band Hamiltonian in the  $\{1-101\}$  representations. The calculations and experiments confirm a facet-induced migration of In during growth that results in a smooth compositional variation from  $x \approx 0.10$  at the bottom of the pyramid to  $x \approx 0.19$  at the top. We demonstrate the existence of a strong correlation between the observed thermal activation behavior and the calculated exciton binding energy for various positions along the pyramidal InGaN/GaN QWs, suggesting exciton dissociation is responsible for the observed temperature dependence of the QW luminescence in the high-temperature range of  $\sim 150$  to 300 K.

#### ACKNOWLEDGMENTS

This work was supported in part by the Israel Science Foundation, NSF, ARO, ONR, and DARPA through the National Center for Integrated Photonic Technology (NCIPT).

- <sup>1</sup>S. Nakamura, M. Senoh, N. Iwasa, S. Nagahama, T. Yamada, and T. Mukai, *Jpn. J. Appl. Phys.* **34**, L1334 (1995).
- <sup>2</sup>S. Nakamura, *IEEE J. Sel. Top. Quantum Electron.* **3**, 712 (1997).
- <sup>3</sup>S. Nakamura and G. Fasol, *The Blue Green Diode* (Springer, Berlin, 1997).
- <sup>4</sup>I. Akasaki and H. Amano, *Jpn. J. Appl. Phys.* **36**, 5393 (1997).
- <sup>5</sup>S. J. Pearton, J. C. Zolper, R. J. Shul, and F. Ren, *J. Appl. Phys.* **86**, 1 (1999).
- <sup>6</sup>P. J. Hansen, Y. E. Strausser, A. N. Erickson, E. J. Tarsa, P. Kozodoy, E. G. Brazel, J. P. Ibbetson, U. Mishra, V. Naraynmurti, S. P. DenBaars, and J. S. Speck, *Appl. Phys. Lett.* **72**, 2247 (1998), and references therein.
- <sup>7</sup>F. A. Ponce, *MRS Bull.* **22**, 51 (1997); S. D. Hersee, J. C. Ramer, and K. J. Malloy, *ibid.* **22**, 45 (1997), and references therein.
- <sup>8</sup>A. Koukitsu, N. Takahashi, T. Taki, and H. Seki, *Jpn. J. Appl. Phys.* **35**, L673 (1996).
- <sup>9</sup>Y. Narukawa, Y. Kawakami, S. Fujita, and S. Nakamura, *Phys. Rev. B* **55**, R1938 (1997).
- <sup>10</sup>K. P. O'Donnell, R. W. Martin, and P. G. Middleton, *Phys. Rev. Lett.* **82**, 237 (1999).
- <sup>11</sup>H. K. Cho, J. Y. Lee, K. S. Kim, and G. M. Yang, *Appl. Phys. Lett.* **77**, 247 (2000).
- <sup>12</sup>S. Chichibu, T. Azuhata, T. Sota, and S. Nakamura, *Appl. Phys. Lett.* **69**, 4188 (1996); *ibid.* **70**, 2822 (1997).
- <sup>13</sup>S. Chichibu, T. Sota, K. Wada, and S. Nakamura, *J. Vac. Sci. Technol. B* **16**, 2204 (1998).
- <sup>14</sup>E. Berkowicz, D. Gershoni, G. Bahir, E. Lakin, D. Shilo, E. Zolotoyabko,

- A. C. Abare, S. P. Denbaars, and L. A. Coldren, *Phys. Rev. B* **61**, 10994 (2000).
- <sup>15</sup>X. Zhang, D. H. Rich, J. T. Kobayashi, N. P. Kobayashi, and P. D. Dapkus, *Appl. Phys. Lett.* **73**, 1430 (1998).
- <sup>16</sup>A. Usui, H. Sunakawa, A. Sakai, and A. Yamaguchi, *Jpn. J. Appl. Phys.* **36**, L899 (1997).
- <sup>17</sup>T. S. Zheleva, O.-H. Nam, M. D. Bremser, and R. F. Davis, *Appl. Phys. Lett.* **71**, 2472 (1997).
- <sup>18</sup>N. P. Kobayashi, J. T. Kobayashi, X. Zhang, P. D. Dapkus, and D. H. Rich, *Appl. Phys. Lett.* **74**, 2836 (1999).
- <sup>19</sup>X. Zhang, P. D. Dapkus, and D. H. Rich, *Appl. Phys. Lett.* **77**, 1496 (2000).
- <sup>20</sup>P. Vennequies, B. Beumont, V. Bousquet, M. Vaille, and P. Gilbert, *J. Appl. Phys.* **87**, 4175 (2000).
- <sup>21</sup>M. Hansen, P. Fini, L. Zhao, A. C. Abare, L. A. Coldren, J. S. Speck, and S. P. DenBaars, *Appl. Phys. Lett.* **76**, 529 (2000).
- <sup>22</sup>X. Zhang, P. D. Dapkus, D. H. Rich, I. Kim, J. T. Kobayashi, and N. P. Kobayashi, *J. Electron. Mater.* **29**, 10 (2000).
- <sup>23</sup>H. T. Lin, D. H. Rich, A. Konkar, P. Chen, and A. Madhukar, *J. Appl. Phys.* **81**, 3186 (1997).
- <sup>24</sup>K. Rammohan, D. H. Rich, R. S. Goldman, J. Chen, H. H. Wieder, and K. L. Kavanagh, *Appl. Phys. Lett.* **66**, 869 (1995).
- <sup>25</sup>K. Rammohan, H. T. Lin, D. H. Rich, and A. Larsson, *J. Appl. Phys.* **78**, 6687 (1995).
- <sup>26</sup>S. N. Mohammad and H. Morkoc, *Prog. Quantum Electron.* **20**, 361 (1996).
- <sup>27</sup>M. Leroux, N. Grandjean, B. Beaumont, G. Nataf, F. Semond, J. Massies, and P. Gibart, *J. Appl. Phys.* **86**, 3721 (1999).
- <sup>28</sup>F. A. Ponce, D. P. Bour, W. Gotz, and P. J. Wright, *Appl. Phys. Lett.* **68**, 57 (1996).
- <sup>29</sup>J. Elsner, R. Jones, M. I. Heggie, P. K. Sitch, M. Haugk, Th. Frauenheim, S. Oberg, and P. R. Briddon, *Phys. Rev. B* **58**, 12571 (1998).
- <sup>30</sup>X. Li, P. W. Bohn, J. Kim, J. O. White, and J. J. Coleman, *Appl. Phys. Lett.* **76**, 3031 (2000).
- <sup>31</sup>C. J. Wu and D. B. Wittry, *J. Appl. Phys.* **49**, 2827 (1978).
- <sup>32</sup>The relationship between carrier concentration  $n_{QW}$  and probe current  $I_b$  is given by  $n_{QW} = I_b E_b \tau_{QW} / 3e E_g \pi r_e^2$ , where  $E_b$  is the e-beam energy,  $E_g$  is the bandgap of GaN,  $r_e$  is the effective lateral radius of the electron-hole plasma generated by the electron beam, and  $\tau_{QW}$  is the carrier lifetime in the QW. For  $E_b = 15$  keV, we take  $r_e = 0.5 \mu\text{m}$  [see T. E. Everhart and P. H. Hoff, *J. Appl. Phys.* **42**, 5837 (1971), for an estimate of the generation volume] and  $\tau_{QW} \approx 2$  ns (for similarly MOCVD-grown QWs in Ref. 15). For large excitation conditions (i.e.,  $I_b > \sim 1$  nA), both  $\tau_{QW}$  and the carrier capture efficiency of the QW may reduce drastically, limiting the applicability of the formula for  $n_{QW}$ .
- <sup>33</sup>J. Rosner, E. C. Carr, M. J. Ludowise, G. Girolami, and H. I. Erikson, *Appl. Phys. Lett.* **70**, 420 (1997).
- <sup>34</sup>M. S. Jeong, Y.-W. Kim, J. O. White, E.-K. Suh, M. G. Cheong, C. S. Kim, C.-H. Hong, and H. J. Lee, *Appl. Phys. Lett.* **79**, 3440 (2001).
- <sup>35</sup>S.-H. Park and S.-L. Chuang, *Phys. Rev. B* **59**, 4725 (1999).
- <sup>36</sup>S.-H. Park, *J. Appl. Phys.* **91**, 9904 (2002).
- <sup>37</sup>K. P. O'Donnell, J. F. W. Mosselmanns, R. W. Martin, S. Pereira, and M. E. White, *J. Phys.: Condens. Matter* **13**, 6977 (2001).
- <sup>38</sup>T. Yang, S. Nakajima, and S. Sakai, *Jpn. J. Appl. Phys.* **34**, 5912 (1995).
- <sup>39</sup>Y. C. Yeo, T. C. Chong, and M. F. Li, *J. Appl. Phys.* **83**, 1429 (1998).
- <sup>40</sup>M. Suzuki, T. Uenoyama, and A. Yanase, *Phys. Rev. B* **52**, 8132 (1995).
- <sup>41</sup>S. L. Chuang and C. S. Chang, *Phys. Rev. B* **54**, 2491 (1996).
- <sup>42</sup>T. Ohtoshi, A. Niwa, and T. Kuroda, *J. Appl. Phys.* **82**, 1518 (1997).
- <sup>43</sup>S. Wei and A. Zunger, *Appl. Phys. Lett.* **69**, 2719 (1996).
- <sup>44</sup>A. F. Wright, *J. Appl. Phys.* **82**, 2833 (1997).
- <sup>45</sup>C. Deger, E. Born, H. Angerer, O. Ambacher, M. Stutzmann, J. Hornsteiner, E. Riha, and G. Fischerauer, *Appl. Phys. Lett.* **72**, 2400 (1998).
- <sup>46</sup>F. Bernardini, V. Fiorentini, and D. Vanderbilt, *Phys. Rev. B* **56**, R10024 (1997).
- <sup>47</sup>A. Zoroddu, F. Bernardini, P. Ruggerone, and V. Fiorentini, *Phys. Rev. B* **64**, 045208 (2001).
- <sup>48</sup>K. E. Brennan and C. J. Summers, *J. Appl. Phys.* **61**, 614 (1987).
- <sup>49</sup>D. C. Hutchings, *Appl. Phys. Lett.* **55**, 1082 (1989).
- <sup>50</sup>R. M. Kolbas and N. Holonyak, *Am. J. Phys.* **52**, 431 (1984).
- <sup>51</sup>E. A. Albaneshi, W. R. L. Lambrecht, and B. Segall, *Mater. Res. Soc. Symp. Proc.*, 339 (1994).
- <sup>52</sup>J.-W. Wu, *Solid State Commun.* **69**, 1057 (1989).
- <sup>53</sup>D. H. Rich, Y. Tang, A. Konkar, P. Chen, and A. Madhukar, *J. Appl. Phys.* **84**, 6337 (1998).
- <sup>54</sup>D. H. Rich, K. C. Rajkumar, L. Chen, A. Madhukar, and F. J. Grunthaner, *Appl. Phys. Lett.* **61**, 222 (1992), and references therein.
- <sup>55</sup>Y. Tang, D. H. Rich, I. Mukhametzanov, P. Chen, and A. Madhukar, *J. Appl. Phys.* **84**, 3342 (1998).